Active remote focus stabilization in oblique plane microscopy

TRUNG DUC NGUYEN,[1] **AMIR RAHMANI,**[2,3] **ALEKS PONJAVIC,**[2,4] **ALFRED MILLETT-SIKKING,**[5] **AND RETO FIOLKA**[1,*]

[1]*Lyda Hill Department of Bioinformatics, UT Southwestern Medical Center, Dallas, TX 75390, USA*
[2]*School of Physics and Astronomy, University of Leeds, Leeds LS2 9JT, UK*
[3]*Bragg Centre for Materials Research, University of Leeds, Leeds LS2 9JT, UK*
[4]*School of Food Science and Nutrition, University of Leeds, Leeds LS2 9JT, UK*
[5]*Calico Life Sciences LLC, South San Francisco, CA 94080, USA*
[*]*Reto.Fiolka@UTSouthwestern.edu*

Abstract: Light-sheet fluorescence microscopy (LSFM) has demonstrated great potential in the life sciences owing to its efficient volumetric imaging capabilities. For long-term imaging, the light-sheet typically needs to be stabilized to the detection focal plane for the best imaging results. Current light-sheet stabilization methods rely on fluorescence emission from the sample, which may interrupt scientific imaging and add to sample photobleaching. Here, we show that for oblique plane microscopes (OPM), a subset of LSFM where a single primary objective is used for illumination and detection, light-sheet stabilization can be achieved without expending sample fluorescence. Our method achieves ~21 nm axial precision and maintains the light-sheet well within the depth of focus of the detection system for hour-long acquisition runs in a lab environment that would otherwise detune the system. We demonstrate subcellular imaging of the actin skeleton in melanoma cancer cells with a stabilized OPM.

1. Introduction

Light-sheet fluorescence microscopy (LSFM) has emerged as a fast and gentle method to acquire volumetric image data [1]. As such, LSFM has found various applications ranging from single-molecule imaging to longitudinal imaging of model organisms. In a typical LSFM implementation, the illumination and detection are implemented through separate objective lenses, oriented at 90 degrees to each other [1]. The system is then carefully aligned such that the light-sheet plane overlaps with the focal plane of the detection system. As such, if the detection objective experiences focal drift (for example through thermal expansion [2]), the relative alignment of the light-sheet and the detection is altered. If left unchecked, the light-sheet can drift outside the depth of focus of the detection system. As a result, the imaging performance of the LSFM is drastically reduced, as predominantly out-of-focus blur is collected. Several "auto-focusing" algorithms have been developed for LSFM [3–5], which typically acquire a series of fluorescence images to estimate the relative displacement. This requires the expenditure of fluorescence for such measurements, and an interruption of the actual imaging operations. This is different to autofocusing systems in conventional, epi-fluorescence microscopes, which typically correct focus drift using a laser beam that is back-reflected from the coverslip [6–8].

Oblique plane microscopy (OPM) is a variant of LSFM which uses a single objective lens at the sample to launch the light-sheet at an oblique angle and detects the fluorescence with the same lens [9,10]. As such, if the primary objective lens exhibits drift, the light-sheet and detection drift at the same rate, and their relative alignment stays intact. The alignment is only broken for higher order aberrations (i.e. imaging in inhomogeneous media), but it can be restored via adaptive optics in an OPM [11].

In a typical OPM, the tilted light-sheet plane is mapped through a remote focusing system [12] onto a camera, which consists of a secondary and tertiary objective. Any drift of the secondary and tertiary objective lenses will shift the detection focal plane, but not the light-sheet (since this is typically coupled into the primary objective without passing the secondary and tertiary objectives). As such, the remote focusing system can cause a similar image degradation as in a conventional LSFM that experiences light-sheet and/or focal plane drift.

Here we show that in an OPM, the remote focusing unit can be stabilized with laser light, which can be spectrally distinct from the fluorescence detection. The system does not need fluorescence light for light-sheet stabilization and runs continuously and independently to fluorescence imaging. This contrasts with light-sheet stabilization in conventional LSFM architectures, which must be interlaced with fluorescence imaging operations. We characterize the precision of the system and demonstrate hour long high resolution OPM imaging of subcellular dynamics.

2. Methods

2.1. Optical setup

In Fig. 1(A), our implementation of OPM is shown. For illumination, laser light from a previously published light-sheet module [13] is coupled over a dichroic mirror (Di03-R405/488/561/635-t1-25 × 36, Semrock) into the optical train of the OPM. After passing through two tube lenses (TL 1: ITL-200, TL2: custom, 150 mm EFL) and two galvo mirrors (Pangolin Saturn 9B with a 10 mm y-mirror mounted 90 degrees rotated) for image space scanning [14], an oblique sheet is launched in sample space through the primary objective (O1, Nikon 40X, NA 1.25 silicone oil).
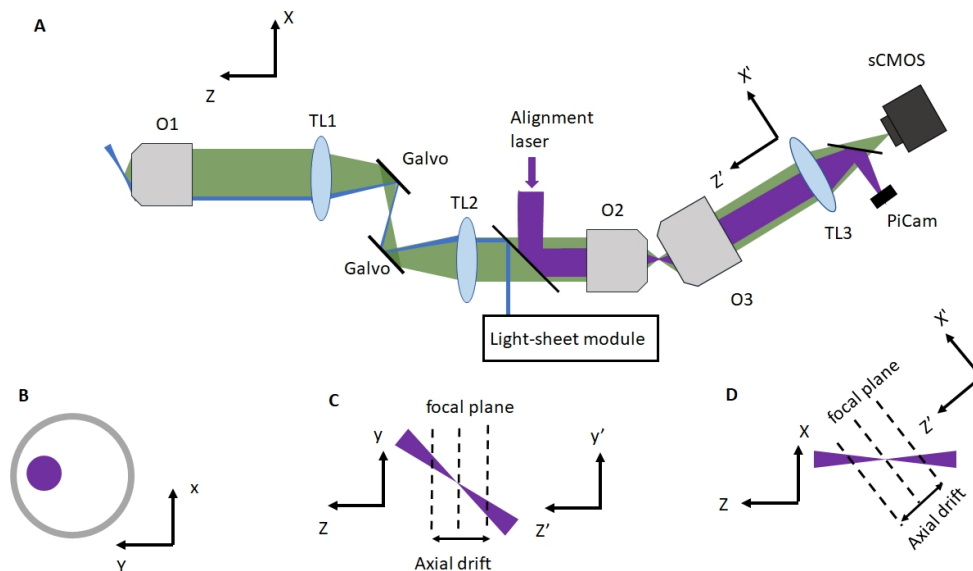
Fig. 1. Schematic layout of an oblique plane microscope (OPM) with remote focus stabilization. **A** Schematic layout of the OPM. Green shows the fluorescence path, blue shows the light-sheet path and magenta shows the alignment laser path. O1: primary objective, O2: secondary objective, O3: tertiary objective. TL1-TL3: first, second and third tube lens. **B** Position of the alignment laser beam (blue) in the pupil of the secondary objective O2. **C** Laser focus in the remote imaging space between O2 and O3. **D** Laser focus shown in an orthogonal plane to **C**. Dotted lines correspond to the focal plane of O3.

Fluorescence light is detected through the same objective, whose pupil is conjugated to the secondary objective (O2, Nikon 40X NA 0.95). The secondary objective maps fluorescence

emitters along the light-sheet into the remote space while minimizing spherical aberrations. A tertiary imaging system is used to map the fluorescence on a scientific CMOS camera (Orca Flash 4, Hamamatsu). The tertiary imaging system consists of a glass-tipped objective (AMS-AGY v2 54-18-9, Applied Scientific instrumentation) and a tube lens (f = 300 mm achromatic doublet, Thorlabs).

For the remote focus stabilization, we injected a collimated laser beam over the backside of the dichroic mirror into the optical train of the OPM (Fig. 1(A)). For the experiments shown here, we used a fiber coupled 488 nm laser (Edmund Optics, 10 mW Pigtailed Laser Diode, part nr: #23-761), which was collimated with a f = 100 mm lens. The alignment laser is attenuated by two neutral density filters (two filters with optical density of 2.0, ND20A, Thorlabs), after which the laser power is reduced to ~10 nW. The reflective side of the dichroic faces towards the primary objective (i.e. the light-sheet illumination laser bounces off the coated front surface of the dichroic). In contrast, the alignment laser first travels through the dichroic mirror substrate. As such, there is a secondary reflection from the substrate itself. We reasoned that if we use a laser line for which the dichroic was optimized for reflection, the secondary reflection would be minor. Indeed, we observed a notable double reflection when using another wavelength (i.e. laser diode at 785 nm), whereas the 488 nm line showed a single dominant reflection. The alignment laser does not contribute significantly to background or crosstalk on the sCMOS camera for fluorescence detection. The dichroic mirror used for pickup and the use of a fluorescence bandpass filter in front of the camera robustly block 488 nm light, both from spurious back reflections from the light-sheet illumination and from the alignment laser.

The alignment laser beam passes through the secondary and tertiary objective and is picked up by a dichroic mirror (Semrock Di02-R488-25 × 36) after the tertiary tube lens. The laser beam is then focused on a camera (OV9281-120, labeled PiCam in Fig. 1(A), or FLIR Grasshopper3 GS3-U3-123S6 M) used for the focus stabilization feedback. While it is advisable to put filters and mirrors in the infinity space, we found that with a tube lens of low optical power, placing the dichroic in the "image space" causes negligible aberrations. Adopters of the technology may consider placing the dichroic in the infinity space of the tertiary imaging system when using a tube lens with shorter focal length.

Our system measures the relative misalignment of the remote focus system by using a laser beam that is tilted to the optical axes of the secondary and tertiary objective (labeled Z and Z' respectively). As such, an axial misalignment not only causes the laser beam to defocus, but also to be translated on the alignment camera. To this end, we inject the alignment beam at an off-center position into the secondary pupil (Fig. 1(B)). This causes the beam to tilt in the remote focus space, as shown in Fig. 1(C). As such, if either the secondary or tertiary objective is shifted axially, i.e. its focal plane moves, the beam is defocused, but also translated laterally along the Y' axis on the alignment camera.

In the other dimension, a tilt of the laser beam occurs naturally, as the tertiary imaging system is angled to the optical axis of the secondary objective (Fig. 1(D)). In case of focal drift of the tertiary objective, the laser beam gets translated in the X' direction, whereas a drift from the secondary objective will not show in the X' direction (see also Fig. 1(D) for an illustration).

The off-centering of the alignment laser in the O2 pupil increases the sensitivity of the measurement (a given focal shift causes a larger lateral shift on the camera), but it also ensures that axial shifts of both O2 and O3 become measurable. To place the laser beam off-center in the pupil of O2, its numerical aperture must be reduced (i.e. the laser beam underfills the pupil). This in turn increases the depth of focus of the laser beam and hence makes fitting of the laser spot easier over a larger defocus range. Importantly, it does not lower the localization precision for the scenario of "unlimited photons". While the spot gets larger in size when reducing its NA, more photons (if the laser intensity of the laser beam is increased accordingly) contribute to the measurement, which restores the measurement precision.

2.2. Feedback control

The feedback control for the remote focus stabilization was implemented on a Rasperry Pi 4B architecture building on the previous PiFocus [6] Python code. The Raspberry Pi continuously acquires a stream of images at 100fps from the PiCam, processes them in real-time to compute an error signal of the laser spot, and uses this signal to control the axial position of the tertiary objective via a piezo stack actuator (PC4GR, Thorlabs, driven by an open loop piezo controller, MDT694B, Thorlabs). The Piezo stack was fitted with a custom mount into a manual 3D stage (Newport 9063-XYZ), where it rests against a differential micrometer.

We implemented a proportional-integral-derivative (PID) controller for fine-tuning the laser spot position and ensuring stabilization. The proportional (P) and integral (I) gains were experimentally optimized to minimize oscillations and suppress displacements of the laser spot. In this implementation, the derivative term was initially set to zero to simplify tuning and prevent overshoot, although it remains an option for future enhancements. The error signal is computed as the Euclidean distance between the current position of the laser spot and its initial calibrated position (setpoint). The position of the laser spot is determined by Gaussian fitting of the 1D projections of the laser intensity distribution (point spread function, PSF) on the x' and y' axes. By summing projections along the x' and y' axes and fitting 1D Gaussian profiles to the data, the system achieves reliable sub-pixel localization of the laser spot even under varying intensity conditions.

For each frame, the PID algorithm operates as follows:

1. Error Calculation:

$$error = \pm\sqrt{(x'_{current} - x'_{setpoint})^2 + (y'_{current} - y'_{setpoint})^2}$$

The sign of the error is determined by the relative position of the current PSF center with respect to the setpoint. In our setup, if the current PSF center $x'_{current}$ is to the left of the setpoint $x'_{setpoint}$ the error is negative. Otherwise, the error is positive. The sign of the output signal (analog voltage to the piezo controller) is determined empirically from the calibration curve.

The proportional gain (K_p) is set to 0.1, the integral gain (K_i) is set to 0.01, and the derivative gain (K_d) is set to 0. With (K_p) set to 0.1, the system compensates for 10% of the error in each iteration. Phrased differently, with the camera's 100fps imaging rate, it could take up to 10 frames (0.1 second) to fully correct for a given error.

2. Control Signal Computation

$$controlSignal = K_p \cdot error + K_i \cdot \int error \, dt + K_d \cdot \frac{d(error)}{dt}$$

- The proportional term (K_p) corrects the displacement magnitude.

- The integral term (K_i) accumulates the error over time, reducing steady-state offset.

- The derivative term (K_d) predicts future errors based on the rate of change, though it was not used in the current implementation to prevent noise amplification.

3. Actuator Update:

The control signal is translated into a voltage adjustment for the piezo stack, ensuring precise axial positioning of the tertiary objective. The corresponding conversion was found by measuring a calibration curve (see also Fig. 2(B)).

We wrote a GUI which allows a user to calibrate the system at the start of an experiment (see also the Supplement 1). In this calibration step, the system captures the initial laser spot
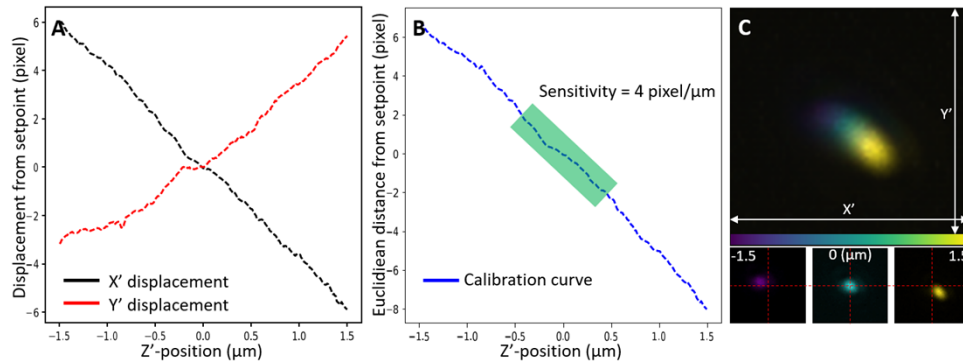
Fig. 2. Axial drift estimation using spatial displacement. **A** X' and Y' displacement of the laser PSF extracted from tertiary objective Z'-scan. **B** Calibration curve of focal drift estimation using Euclidean Distance. **C** Z'-position color-coded projection image of 300 laser spots captured from a tertiary objective scan, insets show the PSFs at -1.5-micron, 0 micron and +1.5 microns. The laser PSF location moves diagonally over the image sensor through the Z'-scan.

position, defining it as the setpoint. Subsequent deviations from this position determine the error signal. The GUI also allows users to adjust critical parameters such as PID gains and verify system alignment. During operation, the system logs the error, control signal, and actuator position for each frame. This data is stored in memory and can be saved as a CSV file for post-experiment analysis. Real-time feedback allows users to monitor the control signal and ensure proper alignment throughout the experiment.

3. Results

3.1. Precision and long-term stability

To measure the precision of our stabilization method, we acquired a rapid timelapse sequence, with a duration of 100 seconds to minimize drift. The standard deviation of the localization measurement of the laser spot was then converted into nanometers using a calibration curve (where the piezo stack was stepped in known increments), as shown in Fig. 2(A)-(C) and Fig. 3(A). We measured a standard deviation of ~28 nm using this approach. If converted back to the sample space (demagnification of 1.33), this corresponds to an axial precision of 21 nm, which is an order of magnitude lower than the depth of focus of the detection system. For comparison, we also performed the same measurements with a FLIR Grasshopper camera, which has a larger bit depth (Supplement 1 and Figure S4). The achievable precision was similar; thus we conclude that photon shot noise is not limiting for our stabilization method, but rather external vibrations in our laboratory.

We measured the long-term stability of the remote focusing system with and without focus stabilization. Without feedback correction, the system exhibited cumulative drift beyond ~5-microns over the course of three hours (Fig. 3(B)). This is not unexpected, as our laboratory experiences temperature oscillations with an amplitude of ~1 degree Celsius (see also Supplement 1 for temperature measurements Figure S5). With the focus stabilization on, the standard deviation over three hours was 37 nm measured in the remote space, corresponding to 28 nm mapped into sample space (Fig. 3(B)).
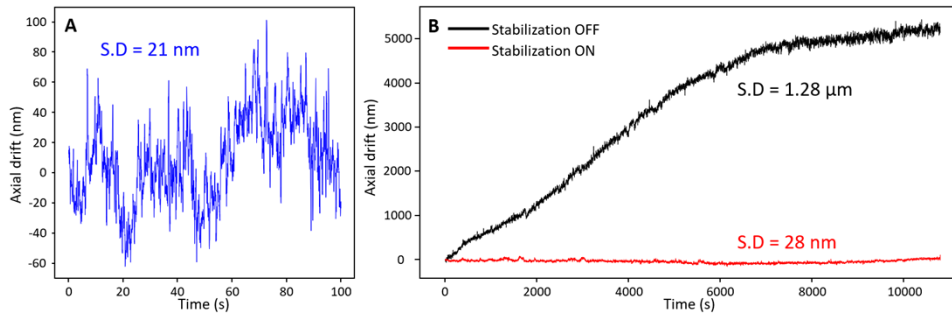
Fig. 3. Axial precision and axial drift with and without remote focus stabilization. **A** Time-lapse acquisition at the focal plane for estimating axial precision using the Raspberry Picam. **B** Axial drift with stabilization ON (red) and OFF (black) monitored for 3 hours. S.D. Standard deviation.

3.2. Imaging of fluorescent nanospheres and melanoma cancer cells

To test the effectiveness of our remote focus stabilization system during OPM imaging operations, we first volumetrically imaged 100 nm diameter fluorescent nanospheres over one hour. In Fig. 4(A)-(B), the first and the last timepoint of volumetric imaging are shown, with the stabilization system turned off. At the beginning of the run, we manually adjusted the light-sheet in respect to the detection for best imaging performance, yielding quite compact point spread functions with little out-of-focus blur (Fig. 4(A)). As evidenced in Fig. 4(B), imaging performance deteriorated after one hour, as the light-sheet no longer overlapped with the detection focal plane, and mainly out-of-focus blur is excited.

In Fig. 4(C)-(D), a second time-lapse imaging experiment is shown, with the stabilization system turned on. The system remained well aligned during the run, as evidenced by the last timepoint shown in Fig. 4(D). We estimated the loss of axial resolution by estimating the axial full width half maximum of the nanosphere images along the two timelapse series. While the remote focus stabilization kept the axial resolution steady (start: 765 nm; end: 820 nm; mean 788 nm; standard deviation: 18 nm), without the stabilization the resolution deteriorated notably (start 775 nm; end: 1148 nm; mean: 1001 nm; standard deviation: 131 nm). In Supplement 1 Figure S6 (see also Supplement 1) we also estimated the loss of lateral resolution using image decorrelation analysis [15]. While with stabilization the lateral resolution stayed steady around 345nm ± 6 nm across the time series, without stabilization the resolution degraded roughly twofold over the course of an hour.

Encouraged by these results, we performed volumetric time-lapse imaging of A375 cancer cells labeled with tractin-mRuby over one hour (2-minute time interval, for a total of 30 volumetric acquisitions) with the stabilization system turned on. Cross-sectional maximum intensity projections at three time points are shown in Fig. 4(F). The data was computationally deconvolved, and the contrast was manually adjusted for each image to compensate for the effect of photobleaching. Fine filopodia are visible on the three cells and remain well resolved during the entire course of the time-lapse acquisition. The raw data for Fig. 4 is included in Dataset 1 [16]. To further illustrate the effects of our stabilization system for biological imaging, we imaged the same fixed ARPE cell labeled for clathrin coated pits over the course of an hour (Supplementary Figure S7 and Dataset 1 [16]) without and with remote focus stabilization.
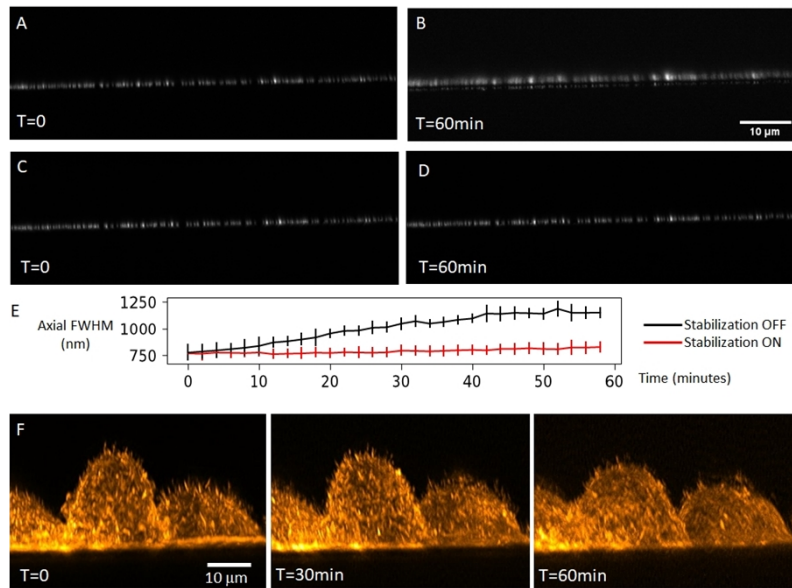
Fig. 4. Time lapse volumetric imaging using OPM with and without remote focus stabilization. **A-B** 100 nm fluorescent nanospheres, as imaged with OPM without remote focus stabilization at the beginning and end of an one hour time lapse series. Cross sectional maximum intensity projections are shown. **C-D** OPM imaging of the same volume as shown in **A-B**, but with remote focus stabilization active. **E** Axial full width half maxima (FWHM) fitted to the nanosphere images in **A-D**. Mean values and standard deviation are displayed. **F** Three timepoints of a timelapse of A375 cancer cells labeled with tractin-mRuby, using OPM with remote focus stabilization active. Cross sectional maximum intensity projections are shown.

4. Discussion

We demonstrate an actively stabilized remote focus scheme that can be implemented in OPM systems with minor modifications. Our scheme greatly increases the long-term performance of an OPM, and compared to other light-sheet modalities, stabilization does not interrupt the imaging operations, nor does it consume fluorescence light.

Improvements to our stabilization method could involve adding PSF engineering to the laser spot. In particular, making the depth sensing independent of the position of the spot on the camera could counter sources of long-term drift. As an example, O3 is mounted on a 3D manual translation stage. If any of its lateral axes (along X' and Y') drift, this would cause a translation of the laser spot on the camera, which could be mis-interpreted as a focal shift. We think that such other sources of drift and vibrations may limit the precision of our setup. Furthermore, they could become limiting for stabilization runs exceeding the three-hour window we presented herein. Another potential limiting factor is the travel range of our piezo actuator, as it could reach its limits (± 10 microns) in some instances. We opted not to use an actuator with more travel range to avoid accidental collisions of the remote focusing objectives. Other OPM implementations using objectives with longer working distances may not face this limitation.

For the imaging experiments presented herein, the stabilization precision was sufficient. However, if more complex light-sheets generated by optical lattices [17], Airy beams [18] or Field Synthesis [19] are used, potentially a higher precision could be desirable, especially for deconvolution. The use of a higher-grade camera may improve the stabilization precision, provided that other external vibrations are kept low. To ease the application of such a system,

we plan to release a plug-in feature for remote focus stabilization in navigate [20], a recent open-source, python based microscope control software.

We did not fix any drift of the primary objective. For volumetric imaging some small axial drift can be tolerated; It simply shifts the volume that is being imaged, without noticeably affecting the imaging point spread function. For instance, the fluorescent nanospheres and cells shifted a few microns downwards in Fig. 5 over the course of an hour. As long as the sample stays within the beam waist of the light-sheet, this drift does not noticeably deteriorate imaging performance. Nevertheless, a secondary focus stabilization [6] for the primary objective could be a valuable addition to an OPM.

Overall, we hope that this resource will find widespread applications in OPM and will enable higher quality data acquisitions over extended time periods.

Disclosures. The authors declare no conflict of interest.

Data availability. The python code for the remote focus stabilization and the raw data underlying Fig. 2,3 is included at [21].

The data underlying Fig. 4 and Supplementary Figure S7 is available at Dataset 1 [16].

Supplemental document. See Supplement 1 for supporting content.

References

1. E. H. Stelzer, F. Strobl, B.-J. Chang, *et al.*, "Light sheet fluorescence microscopy," Nat. Rev. Methods Primers **1**(1), 73 (2021).
2. A. Millett-Sikking, "Focus vs Temperature," Github (2024), retrieved https://github.com/amsikking/Nikon_40x0.95air_focus_vs_temperture.
3. L. A. Royer, W. C. Lemon, R. K. Chhetri, *et al.*, "Adaptive light-sheet microscopy for long-term, high-resolution imaging in living organisms," Nat. Biotechnol. **34**(12), 1267–1278 (2016).
4. L. Silvestri, M. C. Müllenbroich, I. Costantini, *et al.*, "Universal autofocus for quantitative volumetric microscopy of whole mouse brains," Nat. Methods **18**(8), 953–958 (2021).
5. C. Li, A. Moatti, X. Zhang, *et al.*, "Deep learning-based autofocus method enhances image quality in light-sheet fluorescence microscopy," Biomed. Opt. Express **12**(8), 5214–5226 (2021).
6. A. Rahmani, T. Cox, A. T. A. Achary, *et al.*, "Astigmatism-based active focus stabilisation with universal objective lens compatibility, extended operating range and nanometer precision," Opt. Express **32**(8), 13331–13341 (2024).
7. Q. Li, "Autofocus system for microscope," Opt. Eng. **41**(6), 1289 (2002).
8. G. Reinheimer, " Anordnung zum selbsttätigen fokussieren auf in optischen geräten zu betrachtende objekte," (1971).
9. C. Dunsby, "Optically sectioned imaging by oblique plane microscopy," Opt. Express **16**(25), 20306–20316 (2008).
10. M. B. Bouchard, V. Voleti, C. S. Mendes, *et al.*, "Swept confocally-aligned planar excitation (SCAPE) microscopy for high-speed volumetric imaging of behaving organisms," Nat. Photonics **9**(2), 113–119 (2015).
11. C. Mcfadden, Z. Marin, B. Chen, *et al.*, "Adaptive optics in an oblique plane microscope," Biomed. Opt. Express **15**(8), 4498–4512 (2024).
12. E. J. Botcherby, R. Juškaitis, M. J. Booth, *et al.*, "An optical technique for remote focusing in microscopy," Opt. Commun. **281**(4), 880–887 (2008).
13. B. Chen, B.-J. Chang, F. Y. Zhou, *et al.*, "Increasing the field-of-view in oblique plane microscopy via optical tiling," Biomed. Opt. Express **13**(11), 5616–5627 (2022).
14. S. Daetwyler, B.-J. Chang, B. Chen, *et al.*, "Mesoscopic oblique plane microscopy via light-sheet mirroring," Optica **10**(11), 1571–1581 (2023).
15. A. Descloux, K. S. Grußmayer, A. Radenovic, *et al.*, "Parameter-free image resolution estimation based on decorrelation analysis," Nat. Methods **16**(9), 918–924 (2019).
16. T. D. Nguyen, "Image Data," figshare (2024), https://doi.org/10.6084/m9.figshare.28385888.
17. B.-C. Chen, W. R. Legant, K. Wang, *et al.*, "Lattice light-sheet microscopy: imaging molecules to embryos at high spatiotemporal resolution," Science **346**(6208), 1257998 (2014).
18. T. Vettenburg, H. I. C. Dalgarno, J. Nylk, *et al.*, "Light-sheet microscopy using an Airy beam," Nat. Methods **11**(5), 541–544 (2014).

19. B.-J. Chang and R. Fiolka, "Light-sheet engineering using the Field Synthesis theorem," JPhys Photonics **2**(1), 014001 (2020).
20. Z. Marin, X. Wang, D. W. Collison, *et al.*, "Navigate: an open-source platform for smart light-sheet microscopy," Nat. Methods **21**(11), 1967–1969 (2024).
21. T. D. Nguyen, "OPM Autofocus," Github (2024), https://github.com/AdvancedImagingUTSW/OPM-Autofocus.